J. Mech. Phys. Solids 170 (2023) 105095

Contents lists available at ScienceDirect

Journal of the Mechanics and Physics of Solids

journal homepage: www.elsevier.com/locate/jmps

A reduced-order, rotation-based model for thin hard-magnetic plates

Dong Yan, Bastien F.G. Aymon, Pedro M. Reis [*]

Flexible Structures Laboratory, Institute of Mechanical Engineering, École Polytechnique Fédérale de Lausanne, 1015 Lausanne, Switzerland

ARTICLE INFO

Keywords:
Thin plates
Hard magnetorheological elastomers
Reduced-order model
Magnetic potential
Magnetization
Rotation tensor

ABSTRACT

We develop a reduced-order model for thin plates made of hard magnetorheological elastomers (hard-MREs), which are composed of hard-magnetic particles embedded in a polymeric matrix. First, we propose a new magnetic potential, as an alternative to an existing torque-based 3D continuum theory of hard-MREs, obtained by reformulating the remnant magnetization of a deformed hard-MRE body. Specifically, the magnetizations in the initial and current configurations are related by the rotation tensor decomposed from the deformation gradient, independently of stretching deformation, motivated by recently reported observations in microscopic homogenization simulations. Then, we derive a 2D plate model through the dimensional reduction of our proposed rotation-based 3D theory. For comparison, we also provide a second plate model derived from the existing 3D theory. Finally, we perform precision experiments to thoroughly evaluate the proposed 3D and 2D models on hard-magnetic plates under various magnetic and mechanical loading conditions. We demonstrate that our rotation-based modification of the magnetic potential is crucial in correctly capturing the behavior of plates subjected to an applied field aligned with the magnetization, and undergoing in-plane stretching. In all the tested cases, our rotation-based 3D and 2D models yield predictions in excellent quantitative agreement with the experiments and can thus serve as predictive tools for the rational design of hard-magnetic plate structures.

1. Introduction

Soft active materials are compliant to mechanical deformations and responsive to external stimuli, making them ideal candidates for smart structures and systems in applications ranging from sensors and actuators to tissue engineering and energy harvesting (Kim and Zhao, 2022; Wang et al., 2022). This family of materials includes liquid crystal polymers (Wang et al., 2022), shape-memory polymers (Ze et al., 2020), magnetorheological elastomers (MREs) (Kim et al., 2018; Wu et al., 2020; Kim and Zhao, 2022), *etc*. In particular, MREs, consisting of a polymeric matrix embedded with magnetic particles, can change their elastic modulus and morph their shape under magnetic actuation (Danas et al., 2012; Kim et al., 2018). When these materials are embedded with hard-ferromagnetic particles (hard-MREs), the interaction between the applied field and the remnant magnetization of the particles can impose significant torques in the material, leading to large deflections or rotations (Kim et al., 2018; Wu et al., 2020; Kim and Zhao, 2022). The extreme, reversible deformation of structures made of hard-MREs combined with a fast and remote magnetic actuation have recently been leveraged to demonstrate novel functionalities in soft robotics (Kim et al., 2018; Hu et al., 2018; Gu et al., 2020), biomedical engineering devices (Kim et al., 2019; Zhang et al., 2021), flexible electronics (Yan et al., 2021c; Kim and

* Corresponding author.
E-mail addresses: dong.yan@epfl.ch (D. Yan), bastien.aymon@epfl.ch (B.F.G. Aymon), pedro.reis@epfl.ch (P.M. Reis).

https://doi.org/10.1016/j.jmps.2022.105095
Received 20 May 2022; Received in revised form 22 September 2022; Accepted 5 October 2022
Available online 12 October 2022

Zhao, 2022), and metamaterials (Chen et al., 2021). The functionality of those devices can also be customized through the design of a heterogeneous magnetization profile of the MRE (Kim et al., 2018; Lum et al., 2016; Alapan et al., 2020).

Significant effort has been dedicated to modeling hard-MREs towards the rational design of magneto-active systems. Pioneering work dates back to the last century when the theoretical foundations of the field were established within the framework of thermodynamics, continuum mechanics, and electrodynamics to study the response of MREs under magnetic actuation (Truesdell and Toupin, 1960; Brown, 1966; Yih-Hsing and Chau-Shioung, 1973; Pao, 1978). Recently, motivated by engineering applications of mechanical systems with tunable properties (Kordonsky, 1993; Ginder et al., 2000, 2001; Kim et al., 2019; Kim and Zhao, 2022), a variety of magneto-mechanical models for both soft- and hard-MREs (Dorfmann and Ogden, 2003, 2004, 2005; Kankanala and Triantafyllidis, 2004; Zhao et al., 2019; Mukherjee et al., 2020) have been developed by considering, for example, their anisotropy (Danas et al., 2012), viscoelasticity (Rambausek et al., 2022), and magnetic hysteresis (Mukherjee et al., 2021). Also, experiments were performed for the evaluation of coefficients and the validation of the developed models. In particular, Zhao et al. (2019) reported a simple model for hard-MREs with 3D-printed heterogeneous magnetization profiles, building upon past literature on the equilibrium of a deformable solid under magnetic torques and forces (Brown, 1966; Yih-Hsing and Chau-Shioung, 1973). The authors assumed that the hard-MRE was pre-magnetized with a known magnetization profile and a relative permeability close to unity. Another strong assumption was made on the magnetic field, which, in the entire domain, was set to be identical to the externally applied field in vacuum; the influence due to the magnetization of the MRE is neglected. Hence, the problem is reduced to a mechanical problem under magnetic loading (deformation gradient/displacement field is the only independent variable), without the necessity to solve the fully coupled magneto-mechanical equations. This *torque-based* model was validated by several test cases on thin-walled structures deformed under pure magnetic loading (Kim et al., 2018; Zhao et al., 2019), and successfully applied in practical designs (Kim et al., 2019; Kuang et al., 2021). In a follow-up study, Garcia-Gonzalez (2019) extended this torque-based model to the case of hard-magnetic viscoelastic materials. Still using the torque-based continuum theory, Zhang et al. (2020) investigated the micromechanics of hard-MREs with a focus on particle rotation and torque transmission in a representative volume element.

More recently, Mukherjee et al. (2021) have proposed a full-field, microstructurally guided modeling framework for incompressible hard-MREs. The constitutive description was derived with an emphasis on thermodynamic consistency and with parameters determined through homogenization. It is important to highlight that this comprehensive framework can consider the self-field generated by the MRE and the interaction between the microscopic magnetic particles. Unlike preceding models, the magnetic hysteresis of hard-MREs was also considered in the constitutive relations, which enables capturing the nonlinear behavior of hard-MREs under strong magnetic actuation, even above the coercivity of the particles and during the magnetization process. Using this model, the authors analyzed the deformation of an inhomogeneously magnetized cantilever beam in a case where the self-field cannot be neglected. More importantly, their homogenization simulations demonstrated that the magnetization of a bulk pre-magnetized incompressible hard-MRE with a moderately soft matrix is independent of its stretching deformation. This observation is in contradiction with the previous continuum description for the magnetization of a deformed hard-MRE body proposed in Zhao et al. (2019); a critical fact that we will discuss in detail later in this manuscript. Inspired by the work of Mukherjee et al. (2021), Garcia-Gonzalez and Hossain (2021) proposed a microstructural model to study the effect of dipole–dipole interactions on the deformation of hard-MREs, in which only the rotation of the rigid particles is considered to derive the potentials corresponding to the mutual interactions of the particles and the interactions between the external field and the particles. By developing a more comprehensive framework, Rambausek et al. (2022) studied the interplay between the viscoelasticity of the polymeric matrix and the ferromagnetic hysteresis of the particles in hard-MREs.

Building upon the models highlighted above, there have been several studies on the mechanics of magnetic slender structural elements towards enhancing the function of hard-MRE structures through geometry. In pioneering work on thin beams, Lum et al. (2016) developed a 1D model to guide the design of heterogeneous magnetization profiles along the beam axis in order to realize a desired, complex deformation mode (Hu et al., 2018). Starting from the torque-based continuum model, Wang et al. (2020) presented a nonlinear theory of hard-magnetic elastica, which was then used in the design of 1D soft continuum robots (Wang et al., 2021). The numerical implementation and experimental validation of this beam model under a gradient field were performed by Yan et al. (2021a) in a comprehensive study combining reduced-order modeling, 3D finite element modeling, and experiments. A detailed literature review of recent work on magnetic beams can be found in Yan et al. (2021a). By studying 1D structural elements subjected to both bending and twisting, Sano et al. (2022) derived a Kirchhoff-like theory to describe the 3D deformation of hard-magnetic rods. Using this model, the authors investigated the instability of straight and helical rods under magnetic actuation. In addition to beam-like elements, Yan et al. (2021b) developed a 1D axisymmetric model for shells, which was used to rationalize the change of buckling strength of pressurized spherical shells when applying a magnetic field. This 1D shell model was later generalized in a 3D configuration by Pezzulla et al. (2022).

The aforementioned reduced-order models for beams, rods, and shells were all developed using the torque-based theory of hard-MREs proposed by Zhao et al. (2019), ought to its simplicity and proven validity in several configurations (Kim et al., 2018, 2019; Kim and Zhao, 2022). In this existing torque-based 3D theory, as mentioned above, the magnetization of the MRE body in the deformed configuration is related to that in the initial configuration through the deformation gradient, including both stretching and rotational contributions. However, the homogenization simulations performed recently by Mukherjee et al. (2021) on a representative volume element (RVE) showed that the magnetization of hard-MREs remains constant under uniaxial tension perpendicular to pre-magnetization, since the polymeric matrix is much more compliant to the stretching deformation than the metallic particles (which are almost undeformed). The authors concluded that the magnetization of an incompressible hard-MRE depends only on its rotation, independently of stretch (Mukherjee et al., 2021; Garcia-Gonzalez and Hossain, 2021). This microscopic

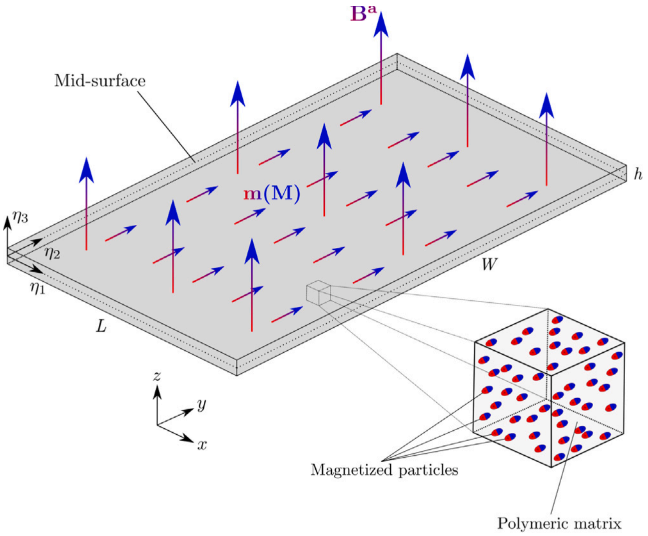

Fig. 1. Schematic of a thin plate made of a hard-MRE in its initial flat configuration, subjected to an external magnetic field $\mathbf{B}^a$. The magnified representative volume element (inset) illustrates the composition of the hard-MRE. The hard-magnetic particles are assumed to have been pre-magnetized, producing the remnant magnetization of the hard-MRE, $\mathbf{m}(\mathbf{M})$.

composite effect was not taken into account by Zhao et al. (2019). Hence, in some cases, the inaccurate description of magnetization might yield an erroneous magnetic part of the Cauchy stress, leading to unreliable predictions on the deformation of the MRE, as we demonstrate in the present study. This issue calls for an effort to update the existing torque-based theory (Zhao et al., 2019) by incorporating the composite effect (Mukherjee et al., 2021). Coming back to slender structures, plates are an essential member of the family in addition to beams, rods, and shells. Even if several promising applications involving magnetic plates have been proposed in the literature (Kim and Zhao, 2022; Hu et al., 2018; Tang et al., 2018; Gray, 2014), their design has been primarily driven by intuition. Thus, there is a timely need for a plate theory to help understand the mechanics of plates under magnetic actuation and support the predictive and rational design of plate-like magneto-elastic structures.

Here, we propose a reduced-order theory for thin plates made of hard-MREs subjected to magnetic and mechanical loading. We start by modifying the existing continuum theory of Zhao et al. (2019), taking into account the independence of magnetization on the stretching deformation of hard-MREs, as pointed out by Mukherjee et al. (2021). We derive a plate model based on this modified 3D theory through a dimensional reduction procedure. Finally, our new 3D and plate theories are validated by comparing simulations against experiments. We shall consider plates actuated by a uniform magnetic field and/or pressurized while systematically varying the loading parameters and boundary conditions. Both the modified 3D model and the developed plate model yield excellent predictions on the deformation of magnetic plates, establishing a basis for the future modeling and design of slender plate-like structures. We note that, to the best of our knowledge, this is the first time a rotation-based model has been validated experimentally for hard-MREs, here using a plate geometry.

Our paper is organized as follows. We define the problem in Section 2. Section 3 reviews the existing torque-based 3D continuum theory (Zhao et al., 2019) and then propose a modified description for the magnetization of a deformed hard-MRE, yielding a rotation-based magnetic potential. In Section 4, a plate model is developed via dimensional reduction of the modified 3D theory. For comparison, we also provide a plate model derived from the existing 3D theory. The numerical implementation is described in Section 5, followed by our experimental methodology in Section 6. In Section 7, we present the experimental results and the comparison between the 3D and 2D models. Finally, the main findings are summarized and discussed in Section 8.

2. Definition of the problem

We consider a thin plate of length L, width W, and thickness h (with $L/h, W/h \gg 1$), as schematized in Fig. 1. The absolute Cartesian coordinate system (x, y, z) is denoted by the base vectors $(\mathbf{e}_1, \mathbf{e}_2, \mathbf{e}_3)$. The plate is parameterized by the in-plane coordinates $\eta_1 \in [0,\ L]$ and $\eta_2 \in [0,\ W]$ in the length and width directions, respectively, and by the out-of-plane coordinate $\eta_3 \in [-h/2,\ h/2]$ along the thickness. The initial flat configuration of the plate is represented by $\mathbf{X} = (\eta_1, \eta_2, \eta_3)$, and the deformed configuration by $\mathbf{x}(\eta_1, \eta_2, \eta_3)$. Throughout the manuscript, capital letters denote quantities written with respect to the original configuration, and lowercase variables refer to the deformed configuration.

The plate is made of a hard-MRE with Young's modulus E and Poisson's ratio ν. The MRE is a two-phase composite made of micron-sized hard-magnetic particles embedded in a non-magnetic elastomeric matrix (Fig. 1, inset). We assume that the diameters of the particles are much smaller than any dimensions of the plate, and that the particles are dispersed evenly in the matrix; the hard-MRE can then be regarded as a homogeneous material. Throughout the present study, we only consider particles that have been pre-magnetized upon saturation with a permeability close to that of vacuum (relative permeability ≈ 1). Consequently, in the initial configuration $\mathbf{X}$, given the magnetization of the individual particles, $\mathbf{M}^{\mathrm{p}}$, and their volume fraction, c, the effective magnetization of the MRE is

$$\mathbf{M} = c\mathbf{M}^{\mathrm{p}} . \tag{1}$$

The counterpart of $\mathbf{M}$ in the deformed configuration $\mathbf{x}$ is $\mathbf{m}$. The magnetization of the MRE is assumed to be independent of external magnetic fields, provided that the MRE is operated under a field strength much smaller than the coercivity of the particles (Zhao et al., 2019). Furthermore, since we are considering thin plates, we can assume $\mathbf{M}$ is constant throughout the thickness.

Under the application of a uniform magnetic field of flux density $\mathbf{B}^{\mathrm{a}}$, magnetic body torques $\boldsymbol{\tau} = \mathbf{m}\times\mathbf{B}^{\mathrm{a}}$ are exerted on the plate. These distributed torques arise from the interaction between the hard-magnetic particles and the external field, transmitted through the matrix. The plate deforms to the current configuration $\mathbf{x}$, with a tendency to align its magnetization to the applied field. We seek to develop a plate model to describe the deformation of a hard-MRE plate under a uniform magnetic field. To do so, we shall first reformulate the magnetic potential of the existing torque-based 3D continuum theory by Zhao et al. (2019), accounting for the composite effect recently studied by Mukherjee et al. (2021). We will then perform a dimensional reduction of the 3D theory to derive a 2D plate model written with respect to the plate mid-surface. Both the reformulated 3D theory and the developed plate model will be validated through precision experiments and compared to the existing 3D theory and the corresponding plate model for completeness.

3. Continuum model of hard-MREs

3.1. The existing torque-based model

In the work of Zhao et al. (2019), the behavior of a bulk hard-MRE under an applied magnetic field was described by a Helmholtz free energy density, including an elastic part, U^{e}, and a magnetic part, U^{m}, as

$$U = U^{\mathrm{e}} + U^{\mathrm{m}} , \tag{2}$$

written with respect to the initial configuration. The magnetic part of the energy density, U^{m} is defined as the potential of the magnetic body torque, $\boldsymbol{\tau} = \mathbf{m}\times\mathbf{B}^{\mathrm{a}}$, imposed on the MRE by the applied field, $\mathbf{B}^{\mathrm{a}}$, that, in the deformed configuration, is written as:

$$u^{\mathrm{m}} = -\mathbf{m}\cdot\mathbf{B}^{\mathrm{a}} , \tag{3}$$

where $\mathbf{m}$ corresponds to the magnetization of the deformed hard-MRE body. Zhao et al. (2019) proposed the relation between $\mathbf{m}$ and its counterpart in the initial configuration, $\mathbf{M}$, to be

$$\mathbf{m} = J^{-1}\mathbf{F}\mathbf{M} , \tag{4}$$

where $\mathbf{F}$ is the deformation gradient and $J = \det(\mathbf{F})$ measures the relative volume change. Then, the density of magnetic potential with respect to the initial configuration is

$$U^{\mathrm{m}}_{\mathbf{F}} = -\mathbf{F}\mathbf{M}\cdot\mathbf{B}^{\mathrm{a}} . \tag{5}$$

This $\mathbf{F}$-based magnetic potential couples the elastic deformation and the magnetic actuation via $\mathbf{F}$; for clarity, the subscript $\mathbf{F}$ is added in $U^{\mathrm{m}}_{\mathbf{F}}$, contrasting to $U^{\mathrm{m}}_{\mathbf{R}}$ introduced below in Eq. (9).

The elastic energy density, U^{e}, introduced in Eq. (2) describes the elastic response of the MRE. Consistently with (Zhao et al., 2019), in the 3D models throughout the present study, we use a neo-Hookean hyperelastic energy density

$$U^{\mathrm{e}} = \frac{G}{2}\left(J^{-2/3}\mathrm{Tr}(\mathbf{F}^{\mathrm{T}}\mathbf{F}) - 3\right) + \frac{K}{2}\left(J-1\right)^2 , \tag{6}$$

where G and K are the shear and bulk moduli of the MRE, respectively, and 'Tr' denotes the trace operator.

3.2. A modified magnetic potential

We now examine the existing model described above, but considering the MRE as a *composite* material, whose effective magnetization arises from the dispersed magnetized particles. Eq. (4) states that the magnetization of a hard-MRE in its deformed configuration is determined by the deformation gradient,

$$\mathbf{F} = \mathbf{R}\mathbf{U} , \tag{7}$$

composed of the stretch, $\mathbf{U}$, and rotation, $\mathbf{R}$, tensors. However, this continuum description is inconsistent with recent observations in homogenization simulations by Mukherjee et al. (2021) on incompressible hard-MREs: the effective magnetization of the deformed MRE depends only on the rotation, irrespective of the stretch, since the individual particles are too stiff to be stretched compared to the matrix phase.

Therefore, we replace $\mathbf{F}$ in Eq. (4) with $\mathbf{R}$, obtaining

$$\mathbf{m} = J^{-1}\mathbf{R}\mathbf{M} = J^{-1}(\mathbf{F}\mathbf{U}^{-1})\mathbf{M} , \tag{8}$$

under the assumption that the matrix is moderately soft (Mukherjee et al., 2021); the rotations of the microscopic particles and the macroscopic MRE remain affine (Vaganov et al., 2018, 2020; Schümann et al., 2021; Zhang et al., 2020). An analytical expression for the inverse of the stretch tensor $\mathbf{U}^{-1}$ as a function of $\mathbf{F}$ is required for the numerics and, for convenience, is provided in Appendix A. Finally, the magnetic potential corresponding to the magnetization in Eq. (8) is

$$U_{\mathbf{R}}^{\mathrm{m}} = -\mathbf{RM} \cdot \mathbf{B}^{\mathrm{a}} . \tag{9}$$

Hereafter, for simplicity, we shall refer to the continuum theory based on the existing magnetic potential in Eq. (5) as the "**F**-*based 3D theory*", and the one based on the modified magnetic potential in Eq. (9) as the "**R**-*based 3D theory*".

4. Reduced-order theory for hard-magnetic plates

We proceed to develop a reduced-order model for thin plates made of hard-MREs, based on the **R**-based 3D theory introduced above. First, we use the classic kinematics of thin plates to compute the rotation of the mid-surface (Section 4.1). Then, we dimensionally reduce the magnetic and mechanical components of the energy potential to the plate mid-surface (Sections 4.2–4.4). Finally, we provide another plate model reduced from the **F**-based 3D theory (Section 4.5), which is compared to the model derived from the **R**-based 3D theory in Section 7.

4.1. Rotation of the mid-surface

Based on the classic kinematics of thin plates (Audoly and Pomeau, 2010), we will specialize the rotation tensor **R** for a thin plate from its deformation gradient **F**, to compute the **R**-based magnetic potential using Eq. (9), noting that this is not a standard procedure. Taking the standard Kirchhoff–Love assumption (Audoly and Pomeau, 2010) – normals to the mid-surface remain normal and unstretched during deformation – the deformed configuration $\mathbf{x}$ of the plate in terms of the mid-surface and its normal vector is $\mathbf{x} = \mathbf{r} + \eta_3\mathbf{n}$, where $\mathbf{r} = (\eta_1 + u_1, \eta_2 + u_2, w)$ is the position vector of the mid-surface of the deformed plate, as a function of the in-plane displacements $u_1(\eta_1, \eta_2)$ and $u_2(\eta_1, \eta_2)$, and out-of-plane displacement $w(\eta_1, \eta_2)$ of the mid-surface. The vector normal to the deformed mid-surface is

$$\mathbf{n} = \frac{\mathbf{r}_{,1} \times \mathbf{r}_{,2}}{|\mathbf{r}_{,1} \times \mathbf{r}_{,2}|} , \tag{10}$$

where $(\cdot)_{,\alpha}$ denotes partial derivation with respect to the (in-plane) mid-surface spatial coordinates η_α ($\alpha = 1, 2$). Hereon, Greek indices (α, β) shall represent the two in-plane directions.

Having defined the initial and deformed configurations, we can compute the deformation gradient as

$$\mathbf{F} = \frac{\partial \mathbf{x}}{\partial \mathbf{X}} = \hat{\mathbf{F}} + \eta_3 \mathbf{n}_{,\alpha} \otimes \mathbf{e}_\alpha , \tag{11}$$

where $\hat{\mathbf{F}} = \mathbf{r}_{,\alpha} \otimes \mathbf{e}_\alpha + \mathbf{n} \otimes \mathbf{e}_3$ is the deformation gradient evaluated at the mid-surface. Hereafter, hatted quantities $\hat{(\cdot)}$ are defined with respect to the plate mid-surface, thus independent of the out-of-plane coordinate η_3. The variation of **F** along the plate thickness is characterized by the term linear in η_3, in Eq. (11).

We now consider the rotation of the plate, which is required to describe the change of magnetization during deformation; see Eq. (8). Note that we derive only the rotation tensor at the mid-surface, $\hat{\mathbf{R}}$, which determines the zero-order term in η_3 of the reduced magnetic potential (see Section 4.3). Since all the nontrivial components of $\hat{\mathbf{F}}^{\mathrm{T}}\hat{\mathbf{F}}$ are planar, we introduce the metric of the deformed mid-surface $\mathbf{g} = (\nabla\mathbf{r})^{\mathrm{T}}\nabla\mathbf{r}$ with $\nabla\mathbf{r} = [\mathbf{r}_{,1}, \mathbf{r}_{,2}]$; a 2×2 symmetric and positive-definite tensor. Then, the rotation tensor at the mid-surface is

$$\hat{\mathbf{R}} = \hat{\mathbf{F}} \begin{pmatrix} \left(\mathbf{g}^{-1/2}\right) & & 0 \\ & & 0 \\ 0 & 0 & 1 \end{pmatrix} , \tag{12}$$

where

$$\mathbf{g}^{-1/2} = -\frac{\left(\mathrm{Tr}(\mathbf{g}) + 2\sqrt{\det(\mathbf{g})}\right)^{\frac{1}{2}}}{\det\left(\mathbf{g} + \sqrt{\det(\mathbf{g})}\mathbf{I}_2\right)} \left[\mathbf{g} + \left(\sqrt{\det(\mathbf{g})} - \mathrm{Tr}(\mathbf{g})\right)\mathbf{I}_2\right] \tag{13}$$

and $\mathbf{I}_2$ is the 2×2 identity matrix. Thus far, we have obtained the mid-surface quantities (functions of only η_1 and η_2) required to describe the deformation and rotation of a thin plate.

4.2. Reduced elastic energy

Classic models for thin elastic plates typically involve the reduction of the 3D energy to a 2D description written with respect to the plate mid-surface. Next, from the classic literature, we first consider the elastic energy, comprising stretching, $\hat{U}^{\mathrm{s}}$, and bending, $\hat{U}^{\mathrm{b}}$, terms. For completeness, we provide their well-established expressions, reduced from the 3D Kirchhoff–Saint Venant energy (Audoly and Pomeau, 2010),

$$\hat{U}^{\mathrm{s}} = \frac{Eh}{2(1-\nu^2)} \left[(1-\nu)E_{\alpha\beta}E_{\alpha\beta} + \nu E_{\alpha\alpha}E_{\beta\beta}\right] , \tag{14}$$

$$\hat{U}^{\mathrm{b}} = \frac{Eh^3}{24(1-\nu^2)}\left[(1-\nu)K_{\alpha\beta}K_{\alpha\beta} + \nu K_{\alpha\alpha}K_{\beta\beta}\right], \tag{15}$$

where E and ν are the Young's modulus and Poisson's ratio of the material, respectively. The in-plane stretching strain in Eq. (14) is

$$\hat{E}_{\alpha\beta} = \frac{1}{2}\left(g_{\alpha\beta} - \delta_{\alpha\beta}\right), \tag{16}$$

and the bending strain in Eq. (15) is

$$\hat{K}_{\alpha\beta} = -\mathbf{r}_{,\alpha} \cdot \mathbf{n}_{,\beta}. \tag{17}$$

Note that this plate model uses the geometrically exact versions of stretching and bending strains for thin plates without neglecting the nonlinear terms. However, given the range of validity of the Kirchhoff–Saint Venant energy, it is expected that the reduced stretching and bending energy terms, given in Eqs. (14) and (15), respectively, and used in our numerical implementation (Section 5), are only valid for small strains and finite rotations. For moderate to large strains, a hyperelastic model would be required.

4.3. Reduced magnetic potential

For the specialization of the 3D magnetic potential proposed in Eq. (9) to a thin plate, we need to substitute the rotation tensor $\mathbf{R}$ of Eq. (7) into $U^{\mathrm{m}}_{\mathbf{R}}$ in Eq. (9), and integrate over the thickness. Here, we take only the zero-order term of $U^{\mathrm{m}}_{\mathbf{R}}$ in η_3, to obtain the reduced magnetic potential of the plate as:

$$\hat{U}^{\mathrm{m}}_{\mathbf{R}} = \int_{-h/2}^{h/2} U^{\mathrm{m}}_{\mathbf{R}}|_{\eta_3=0}\, \mathrm{d}\eta_3 = -h(\hat{\mathbf{R}}\mathbf{M}) \cdot \mathbf{B}^{\mathrm{a}}, \tag{18}$$

which is linear to the thickness. In Section 7, the adequacy of neglecting high-order terms in η_3 will be validated against experiments, in a variety of test cases. Also, note that in recent work on hard-magnetic beams (Yan et al., 2021a), rods (Sano et al., 2022), and shells (Yan et al., 2021b), the zero-order term of the magnetic potential was deemed sufficient to describe the mechanics of these structures under magnetic actuation.

4.4. Plate model constructed using the R-based 3D theory

Summing the 2D elastic and magnetic energy potentials integrated over the mid-surface S yields the total energy of the plate

$$\hat{\mathcal{U}}_{\mathbf{R}} = \int_S \left(\hat{U}^{\mathrm{s}} + \hat{U}^{\mathrm{b}} + \hat{U}^{\mathrm{m}}_{\mathbf{R}}\right) \mathrm{d}S, \tag{19}$$

which is a functional of the displacement fields of the mid-surface $(u_1(\eta_1,\eta_2),\, u_2(\eta_1,\eta_2),\, w(\eta_1,\eta_2))$. Therefore, the problem has been reduced from a bulk description (3D) to the mid-surface (2D). Since the model is constructed from the **R**-based 3D theory, we refer to it as the **R**-based plate model. Under given boundary conditions, we can solve for the displacements of the mid-surface by minimizing the energy functional in Eq. (19), which, in this work, we conduct numerically using the finite element method (see Section 5).

4.5. Alternative plate model derived from the F-based 3D theory

Following a dimensional reduction procedure similar to that presented in Sections 4.2–4.4, an alternative plate model can be derived from the existing **F**-based 3D theory (Zhao et al., 2019). The corresponding reduced magnetic potential written with respect to the plate mid-surface is (see Appendix B for details)

$$\hat{U}^{\mathrm{m}}_{\mathbf{F}} = -h(\hat{\mathbf{F}}\mathbf{M}) \cdot \mathbf{B}^{\mathrm{a}}. \tag{20}$$

Using $\hat{U}^{\mathrm{s}}$ and $\hat{U}^{\mathrm{b}}$ from Eqs. (14) and (15), respectively, the reduced total energy potential of the plate is

$$\hat{\mathcal{U}}_{\mathbf{F}} = \int_S \left(\hat{U}^{\mathrm{s}} + \hat{U}^{\mathrm{b}} + \hat{U}^{\mathrm{m}}_{\mathbf{F}}\right) \mathrm{d}S. \tag{21}$$

Comparing $\hat{U}^{\mathrm{m}}_{\mathbf{R}}$ in Eq. (18) with $\hat{U}^{\mathrm{m}}_{\mathbf{F}}$ in Eq. (20), we highlight that $\hat{U}^{\mathrm{m}}_{\mathbf{R}}$ depends only on the rotation of the mid-surface $\hat{\mathbf{R}}$, independently of the stretch $\hat{\mathbf{U}}$. Hence, in general, $\hat{U}^{\mathrm{m}}_{\mathbf{R}} \neq \hat{U}^{\mathrm{m}}_{\mathbf{F}}$. We also notice that, for thin plates, the normal and shear strains in the out-of-plane direction vanish under the Kirchhoff–Love assumption. Consequently, one can verify that, when the initial magnetization $\mathbf{M}$ is parallel to $\mathbf{e}_3$, $\hat{U}^{\mathrm{m}}_{\mathbf{R}}$ and $\hat{U}^{\mathrm{m}}_{\mathbf{F}}$ are identical. In Section 7, the two reduced-order plate models based on either $\hat{U}^{\mathrm{m}}_{\mathbf{R}}$ or $\hat{U}^{\mathrm{m}}_{\mathbf{F}}$ will be examined thoroughly and compared against experiments in a series of test cases.

5. Numerical implementation of the bulk and plate models

The numerical implementation was performed using the commercial software package COMSOL Multiphysics, solving for the displacement fields of the plate by minimizing the energy functional under given boundary conditions, using the finite element method (FEM). In the following, we provide details on the energy functional corresponding to each model and the parameters used in the simulations.

5.1. Simulations using the R-based and F-based 3D models

For the 3D simulations, we consider a volumetric domain occupied by a plate of length L, width W, and thickness h. The total plate energy includes elastic and magnetic parts: for the former, U^{e}, we use the neo-Hookean model in Eq. (6) and for the latter we choose either $U^{\mathrm{m}}_{\mathbf{R}}$ of Eq. (9) for the **R**-based 3D theory proposed in Section 3.2, or $U^{\mathrm{m}}_{\mathbf{F}}$ of Eq. (5) for the **F**-based 3D theory of Zhao et al. (2019). In addition to elastic and magnetic effects, we also consider the self-weight effects present in the experiments through the potential

$$U^{\mathrm{g}} = -\rho \mathbf{g} \cdot \mathbf{x}\,, \tag{22}$$

where ρ is the material density and $\mathbf{g}$ is gravitational acceleration. When a uniform pressure is applied perpendicular to the surface of the plate (Sections 7.4 and 7.5), we add the potential of a dead pressure p:

$$U^{\mathrm{p}} = -p(\mathbf{x} - \mathbf{X}) \cdot \mathrm{e}_3\,. \tag{23}$$

All in all, the energy functional considered in our numerics for the **R**-based 3D theory is

$$\mathcal{U}_{\mathbf{R}} = \int_V \left(U^{\mathrm{e}} + U^{\mathrm{m}}_{\mathbf{R}} + U^{\mathrm{g}}\right)\,\mathrm{d}V + \int_{S^{\mathrm{p}}} U^{\mathrm{p}}\,\mathrm{d}S^{\mathrm{p}}\,, \tag{24}$$

and for the **F**-based 3D theory, we have

$$\mathcal{U}_{\mathbf{F}} = \int_V \left(U^{\mathrm{e}} + U^{\mathrm{m}}_{\mathbf{F}} + U^{\mathrm{g}}\right)\,\mathrm{d}V + \int_{S^{\mathrm{p}}} U^{\mathrm{p}}\,\mathrm{d}S^{\mathrm{p}}\,, \tag{25}$$

where V is the reference volume of the 3D body, and S^{p} is the reference area of the surface on which the pressure is applied.

To minimize $\mathcal{U}_{\mathbf{R}}$ or $\mathcal{U}_{\mathbf{F}}$ numerically, the plate was discretized by a structured mesh with $40 \times 40 \times 8$ hexahedron elements seeded evenly in the length, width, and thickness directions, respectively. We used the cubic Hermite shape function. A mesh convergence study was conducted to ensure that the results were independent of the discretization. All geometric, elastic, and magnetic parameters used in the simulations were characterized independently in experiments (see Section 6); there are no fitting parameters.

5.2. Simulations using the R-based and F-based plate models

In simulations using the dimensionally reduced plate models we consider only the 2D mid-surface, S, of the plate. In addition to the reduced stretching energy, $\hat{U}^{\mathrm{s}}$ (Eq. (14)), bending energy, $\hat{U}^{\mathrm{b}}$ (Eq. (15)), and magnetic potential, $\hat{U}^{\mathrm{m}}_{\mathbf{R}}$ (Eq. (18)) or $\hat{U}^{\mathrm{m}}_{\mathbf{F}}$ (Eq. (20)), the gravitational potential of the plate is

$$\hat{U}^{\mathrm{g}} = -h\rho \mathbf{g} \cdot \mathbf{r}\,. \tag{26}$$

When pressure loading is also imposed (Sections 7.4 and 7.5), the potential of a dead pressure p is

$$\hat{U}^{\mathrm{p}} = -pw\,. \tag{27}$$

Combining the above information, the energy functionals corresponding to the **R**-based (Section 4.4) and **F**-based (Section 4.5) plate models are, respectively,

$$\hat{\mathcal{U}}_{\mathbf{R}} = \int_S \left(\hat{U}^{\mathrm{s}} + \hat{U}^{\mathrm{b}} + \hat{U}^{\mathrm{m}}_{\mathbf{R}} + \hat{U}^{\mathrm{g}}\right)\,\mathrm{d}S + \int_{S^{\mathrm{p}}} \hat{U}^{\mathrm{p}}\,\mathrm{d}S^{\mathrm{p}}\,, \tag{28}$$

and

$$\hat{\mathcal{U}}_{\mathbf{F}} = \int_S \left(\hat{U}^{\mathrm{s}} + \hat{U}^{\mathrm{b}} + \hat{U}^{\mathrm{m}}_{\mathbf{F}} + \hat{U}^{\mathrm{g}}\right)\,\mathrm{d}S + \int_{S^{\mathrm{p}}} \hat{U}^{\mathrm{p}}\,\mathrm{d}S^{\mathrm{p}}\,. \tag{29}$$

The displacements predicted by these two plate models were obtained numerically by minimizing $\hat{\mathcal{U}}_{\mathbf{R}}$ and $\hat{\mathcal{U}}_{\mathbf{F}}$ with respect to the displacement fields. These simulations were performed using COMSOL Multiphysics, discretizing the 2D domain (plate mid-surface) with 6282 triangular elements (50 nodes on each edge), using the quintic Argyris shape function (Argyris et al., 1968; Pezzulla et al., 2022), after a mesh convergence study. Constraints on displacements and their derivatives were specified on the plate edges, when required.

6. Experimental fabrication, apparatus and protocols

To validate the theoretical models introduced in Section 4 and their numerical implementations presented in Section 5, we performed an experimental campaign on thin plate specimens made of hard-MREs, in a variety of test cases, and examined their deformations under different loading conditions. The detailed comparison between the numerical and experimental results will be provided in Section 7. In the present section, we elaborate on our experimental protocols for specimen fabrication, field generation, and deformation measurements.

Table 1
Dimensions and properties of the specimens and levels of the magnetic field and air pressure applied.

Section	L [mm]	h [μm]	E [MPa]	ρ [g/cm^3]	M [kA/m]	B^a [mT]	p [Pa]
Section 7.1	25.2	481	1.15	2.00	90.2	$[0, 20]$	–
Section 7.2	42.0	869	1.81	2.03	91.3	$[0, 15]$	–
Section 7.3	25.2	487	1.15	2.00	90.2	$[0, 60]$	–
Section 7.4	25.0	520	1.07	2.00	90.2	$[0, 100]$	$[0, 300]$
Section 7.5	25.0	505	1.15	2.00	90.2	$[0, 160]$	$[0, 400]$

6.1. Fabrication of hard-MRE plates

The hard-MRE were prepared following a well-established procedure (Yan et al., 2021a,b; Lum et al., 2016): vinylpolysiloxane (VPS) was mixed with NdPrFeB particles (average size 5 μm, MQFP-15-7-20065-089, Magnequench). Depending on the desired Young's modulus, E of the MRE, we used either VPS-22 (Elite Double 22, Zhermack, $E \approx 0.8$ MPa) or VPS-32 (Elite Double 32, Zhermack, $E \approx 1.2$ MPa). The *NdPrFeB:VPS-catalyst:VPS-base* mass ratio was 2:1:1. Hereon, MREs made of VPS-22 or VPS-32 shall be referenced as MRE-22 or MRE-32, respectively.

The plate specimens were fabricated using the liquid MRE prepared as described above, through film application or casting. We used a thin film applicator (ZAA 2300, Zehntner) to fabricate the hard-MRE plates of thickness $481 \le h \le 520\,\mu\text{m}$, as listed in Table 1. We waited for 3 min after the mixture preparation to increase the viscosity to a desired value. The mixture was then poured onto a glass platform and spread by an automated moving applicator (speed 5 mm/s), with a gap height set to 750 μm. The MRE film was left to cure on the glass platform for 20 min. The final thickness depended on the combination of the mixture's viscosity, the applicator's moving speed, and the height of the gap between the applicator and the glass platform. The hard-MRE plate of thickness $h = 869\,\mu\text{m}$ (see Table 1) was cast using a square acrylic frame placed on a glass platform as a mold. The liquid MRE was poured into the frame immediately after the preparation of the MRE mixture. The thickness was controlled by the volume of the liquid MRE poured.

Upon curing, the MRE plate was peeled off from the film applicator or the mold, and square specimens of the desired length L were cut using a scalpel. The specimens' thickness was measured using a microscope (VHX-5000, Keyence) as reported in Table 1, together with the respective Section where the corresponding results are presented. The specimens were then magnetized by saturating the embedded NdPrFeB particles up to 96% under the axial magnetic field (≈ 2.5 T) generated by a pulse magnetizer (IM-K-010020-A, Magnet-Physik Dr. Steingroever). To do so, each specimen was positioned precisely in the magnetizing coil (MF-AsA-ϕ120 × 120,0 mm, Magnet-Physik Dr. Steingroever) such that the desired orientation of magnetization (along or across the thickness of the plate, see Section 7) was aligned with the coil axis.

The volume fraction of the particles was set to 13.2% for MRE-22 and 13.3% for MRE-32. The density of the MRE was $\rho = 2.00\,\text{g/cm}^3$ for MRE-22 and $\rho = 2.03\,\text{g/cm}^3$ for MRE-32. The volume-average magnetization of the MRE was $M = 90.2$ kA/m for MRE-22 and $M = 91.3$ kA/m for MRE-32, given the volume fraction and magnetization of the particles (685.3 kA/m at 96% saturation, from the supplier).

The elastic properties of the MRE were characterized by mechanical testing of standard dogbone specimens under axial tension. Considering the evolution of Young's modulus over time, the dogbone tests and the plate experiments were both conducted at a specific time after the specimen fabrication. The Young's modulus of MRE-22 was measured to be 1.07 MPa at 48 h, increasing to 1.15 MPa at 72 h. For MRE-32, it was 1.81 MPa at 48 h. The reported value is the average of 2 independent tests on 2 dogbone specimens. The Young's moduli corresponding to the plate specimens used in Section 7 are also summarized in Table 1.

6.2. Generation of the magnetic and pressure loading

The magnetic field applied on the plate specimens was generated by two circular electromagnetic coils set in a Helmholtz configuration, powered by two 1.5 kW DC power supplies (EA-PSI 9200-25 T, EA-Elektro-Automatik). This magnetic field was axial and uniform in the central region between the coils. The setup we used was similar to that reported in Yan et al. (2021a) but with coils of different sizes. Here, we chose a pair of bigger coils (inner diameter 190 mm, outer diameter 283 mm, height 54 mm) or a pair of small coils (inner diameter 86 mm, outer diameter 152 mm, height 33 mm) depending on the size of the specimen. We ensured that the specimen deformed within the uniform region of the field. The field strength was characterized using a Teslameter (FH 55, Magnet-Physik Dr. Steingroever). The ranges of the field strength for each experiment are listed in Table 1.

For the experiments also involving pressure loading, we applied a uniform pressure on the plate surface through an air chamber connected to a pneumatic loading system (see Sections 7.4 and 7.5). The pressure differential was produced by injecting air into the chamber using a syringe pump (NE-1000, New Era Pump Systems Inc.) at the constant flow rate of 0.8 mL/min to increase (or decrease) the internal pressure. This pressure differential was monitored by a pressure sensor (785-HSCDRRN005NDAA5, Honeywell International Inc.) at an acquisition rate of 8 Hz.

6.3. Measurement of plate deflections

The deflection of the loaded plates was measured using a camera (Sections 7.1–7.3) or a position sensor (Sections 7.4 and 7.5), depending on its extent. For deflections much larger than the plate thickness, the deformed configuration was captured by a camera (Nikon D850). The displacements at different loading levels were then acquired through digital image processing in MATLAB. For deflections of the order of the plate thickness, an optical position sensor (CL6-MG20, CCS-Optima+, STIL) with a resolution of $0.8\,\mu\mathrm{m}$ was used to directly measure the out-of-plane displacement.

7. Results: Validation of the R-based and F-based models against experiments

We proceed by presenting a series of test cases designed to validate the models introduced above. Our goal is to compare the performance of the **R**-based and **F**-based models in predicting the deformation of hard-MRE plates magnetized and loaded in different configurations. We also aim to identify the conditions where the **R**-based models outperform the **F**-based models in terms of the accuracy. Thus, in each test case, the predictions from the 3D and 2D models developed in Sections 3 and 4 are compared against experimental measurements. We highlight that the geometric, elastic, and magnetic properties used in the simulations have been either characterized experimentally (Section 6) or given by providers, and, thus, with no fitting parameters.

7.1. Deflection of a suspended plate clamped at one edge

First, we consider a square plate magnetized in-plane with $\mathbf{M} = -M\mathbf{e}_2$ and suspended under gravity; see Fig. 2(a). By applying a uniform magnetic field $\mathbf{B}^{\mathrm{a}} = \pm B^{\mathrm{a}}\mathbf{e}_3$, perpendicular to the plate magnetization in the initial configuration, magnetic torques are generated throughout the plate. Consequently, the plate deflects; see the representative photographs of Fig. 2(b1)–(b3), captured at different field strengths. We performed the same test on three identical specimens, and each was tested twice with the field in the z or $-z$ directions, respectively, to reduce positioning errors. The absolute values of the deflection were extracted from the experimental photographs, and the reported data is the average of the six independent measurements.

In Fig. 2(c), we plot the deflection of the bottom edge of the plate in the y and z directions, δ_y/h and δ_z/h (normalized by the plate thickness), as a function of the magnetic flux density B^{a}. The curves are monotonic but highly nonlinear for large deflections, due to the geometric nonlinearity and the dependence of magnetic torques on the rotation of the plate. When the magnetization of the majority of the plate is aligned with the external field, the curves reach a plateau. In this first test case, both the **F**-based and the **R**-based models yield results in excellent agreement with the experiments. Since both the 3D and 2D models are geometrically nonlinear, the large deflections considered can be predicted accurately. In particular, we superimpose the deformed configurations as predicted by the **R**-based plate model on the corresponding plate specimen in each photograph shown in Fig. 2(b1)–(b3), observing excellent agreement throughout.

7.2. Deflection of a plate clamped at two edges

In a second test case, we consider a square plate clamped at two of its boundaries; see Fig. 3(a). The plate is pre-magnetized in-plane and diagonally, *i.e.*, $\mathbf{M} = -M\mathbf{e}_2$. The lower part of plate deflects due to magnetic body torques imposed by a uniform magnetic field $\mathbf{B^a}$ applied in the out-of-plane direction. Fig. 3(b1)–(b3) show representative experimental photographs with increasing field flux density. We tested three identical specimens, each deflected in the z and $-z$ directions under the field of $\mathbf{B^a} = B^a\mathbf{e}_3$ and $\mathbf{B^a} = -B^a\mathbf{e}_3$, respectively. The absolute values of the deflection were extracted from the experimental photographs.

In Fig. 3(c), we plot the average deflection at the free corner of the plate, δ_y/h and δ_z/h (normalized by its thickness in the y and z directions), as a function of B^{a}. The deflections measured in this test case reach up to nearly 30 times the plate thickness, and are predicted well by all the models. This can also be seen in the comparison between the deformed configurations of the plate captured in the experiment and predicted by the **R**-based plate model; see Fig. 3(b1)–(b3).

Through this test case and the one in Section 7.1, we have validated the ability of all our models to describe the large deflection of hard-MRE plates with geometric nonlinearities. In particular, we have demonstrated that our dimensional reduction procedure yields results just as accurate as the 3D models. Since the deformation considered so far is bending-dominated with negligible stretching deformation of the mid-surface, there is no significant difference between the **R**-based and **F**-based models.

7.3. Deflection of a plate clamped at three edges

Hereon, the excited modes of deformation will involve stretching of the mid-surface of a square plate clamped at three edges; see Fig. 4(a). We have introduced in-plane, symmetric magnetization vectors of equal magnitude facing the middle of the plate. Experimentally, this was achieved by folding the plate in half during magnetization. A uniform magnetic field $\mathbf{B^a}$ is applied in the out-of-plane direction to deflect the plate, inducing both bending and stretching deformations. We present representative experimental photographs in Fig. 4(b1)–(b3) at three loading levels. Three identical specimens were tested under both $\mathbf{B^a} = B^a\mathbf{e}_3$ and $\mathbf{B^a} = -B^a\mathbf{e}_3$, and the deflections were extracted from the photographs.

Fig. 4(c) presents the averaged normalized deflection at the midpoint of the free edge, δ_z/h, as a function of B^{a}. Despite the good agreement with experiments, we notice a small difference between the **F**-based and **R**-based models, which becomes more prominent as the deflection increases. This discrepancy is due to the different descriptions on the magnetization of the deformed plate (see Eqs. (4) and (8)), as we have detailed in Section 3. However, the differences in the predictions of the two families of models are not yet significant enough to state that the **R**-based models perform better.

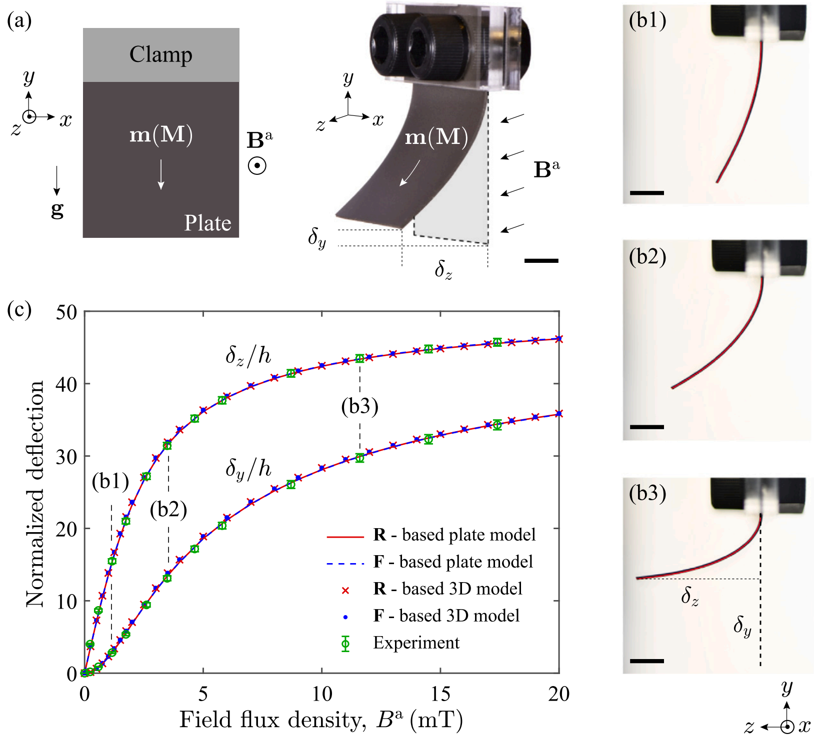

Fig. 2. Deformation of a suspended square plate under a uniform magnetic field. (a) Left: Schematic diagram in the x–y plane. Right: Photograph of a plate specimen tested, with its top edge clamped between rigid plates. The gravitational field $\mathbf{g}$ points in the $-y$ direction. (b) Experimental photographs (side view: $y-z$ plane) of the deformed plate at different levels of magnetic flux density: (b1) $B^a = 1.2\,\mathrm{mT}$, (b2) $B^a = 3.5\,\mathrm{mT}$, and (b3) $B^a = 12\,\mathrm{mT}$. The red lines in each photograph are the deformed configurations predicted by the **R**-based plate model. (c) Normalized components of the deflection at the bottom edge of the plate, δ_y/h and δ_z/h, versus magnetic flux density B^a. The error bars of the experimental data correspond to the standard deviations of the measurements on three identical specimens. The labeled points correspond to the photographs in (b1), (b2), and (b3) for the respective values of B^a. The dimensions of the specimen are provided in Table 1.

7.4. Deflection of a pressurized, fully-clamped plate with in-plane magnetization

We further validate our models by considering another test case where the external magnetic field is aligned with the plate magnetization in the initial configuration, which shall emphasize the difference between the **F**-based and the **R**-based models. A square plate is fully clamped on its four boundaries, we set the magnetization $\mathbf{M} = M\mathbf{e}_2$, and apply a uniform field $\mathbf{B}^a = B^a\mathbf{e}_2$ aligned with **M**. Fig. 5(a) and (b) show a photograph and a schematic of the setup. The two vectors $\mathbf{B}^a$ and **M** are oriented in-plane and parallel in the initial configuration. We then impose a uniform pressure on the plate to introduce both bending and stretching deformation in the presence of the magnetic field. The field strength is kept constant, but the pressure is swept from 0 to 300 Pa. The plate deflection induces an angle between $\mathbf{B}^a$ and **M**, resulting in magnetic torques that oppose the deformation. We quantify this pressure-induced, magnetically-restricted deformation by examining the deflection of the pressurized plate at different levels of B^a. Since the deflection is now smaller (of the order of the plate thickness) than that in the previous test cases, we used a position sensor (see Section 6.3).

Fig. 5(c) and (d) show the deflection at the center of the plate normalized by the plate thickness, δ_z/h, as a function of pressure, p, with and without the external magnetic field, *i.e.*, $B^a = \{0, 100\}\,\mathrm{mT}$. First, we focus on the experimental data and the predictions obtained through the **R**-based 2D and 3D models in Fig. 5(c), finding excellent agreement between theory and experiments. We highlight that, at a given level of pressure loading, the plate deflection decreases with increasing magnetic flux density; the magnetic torques generated by the applied magnetic field act on the plate to keep it flat, in competition with the applied pressure.

Having validated the **R**-based models, we turn to compare the experiments with the predictions from the **F**-based models. From the data in Fig. 5(d), in the presence of a magnetic field ($B^a = 100\,\mathrm{mT}$), we find that both the **F**-based 3D and plate models deviate significantly from the experiments, even for small deflections ($\delta_z/h < 1$). Specifically, the predicted deflections at $B^a = 100\,\mathrm{mT}$ show negligible changes from the $B^a = 0\,\mathrm{mT}$ case. The fact that the deflections are independent of the magnetic field indicates that the stretch part of the deformation gradient suppresses the magnetic effect induced by the rotation part. This disagreement suggests that the accuracy of the **F**-based models worsens considerably when the plate deflects with stretching deformation in the presence of an applied field parallel to the magnetization. These results are a first step towards validating the independence of magnetization on stretching deformation reported by Mukherjee et al. (2021) through homogenization simulations, which will be further examined in

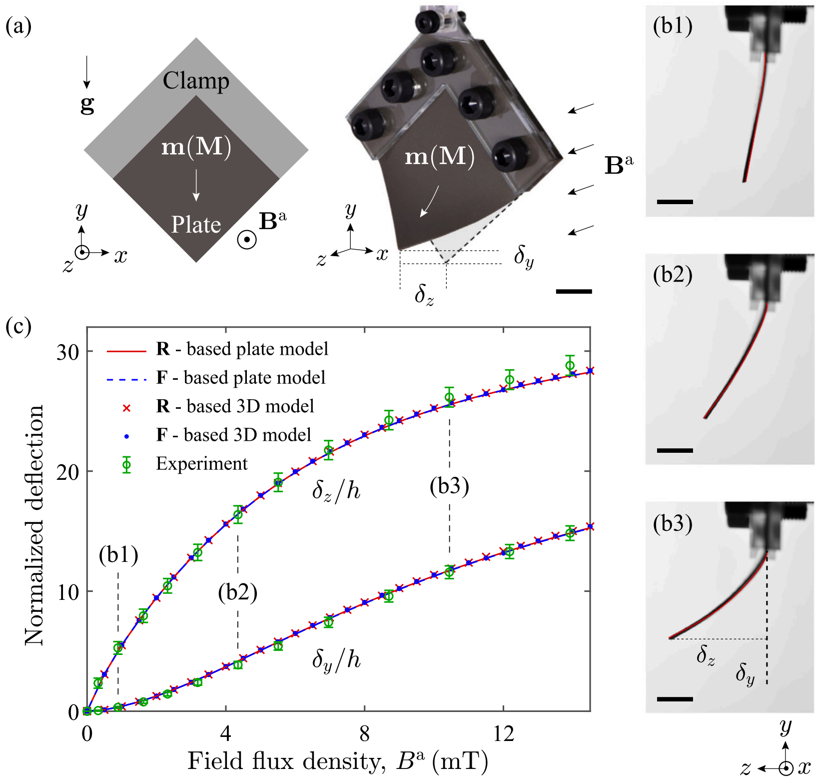

Fig. 3. Deformation of a plate clamped at two edges under a uniform magnetic field. (a) Left: Schematic diagram in the x–y plane. Right: Photograph of a plate specimen, with two edges clamped between rigid plates. The gravitational field $\mathbf{g}$ points in the $-y$ direction. (b) Experimental photographs (side view: $y-z$ plane) of the deformed plate at different levels of magnetic flux density: (b1) $B^{\mathrm{a}} = 0.9\,\mathrm{mT}$, (b2) $B^{\mathrm{a}} = 4.4\,\mathrm{mT}$, and (b3) $B^{\mathrm{a}} = 10\,\mathrm{mT}$. The red lines in each photograph are the deformed configurations predicted by the **R**-based plate model. (c) Normalized components of the deflection at the free corner of the plate, δ_y/h and δ_z/h, versus magnetic flux density B^{a}. The error bars correspond to the standard deviations of the measurements on three identical specimens. The labeled points correspond to the photographs in (b1), (b2), and (b3) for the respective values of B^{a}. The dimensions of the specimen are provided in Table 1.

the next section. We also remark that, for the case of an applied field antiparallel to the magnetization, which was not considered in the study above, the plate is unstable in the flat configuration. This instability and change in the plate deformation mode could be an interesting topic for future studies.

7.5. Deflection of a pressurized, fully-clamped plate with out-of-plane magnetization

In our last test case, we further examine the effect of stretching deformation when a magnetic field $\mathbf{B}^{\mathrm{a}}$ is applied parallel to the plate magnetization $\mathbf{M}$, but we now set $\mathbf{B}^{\mathrm{a}}$ and $\mathbf{M}$ in the out-of-plane direction. Fig. 6(a) and (b) present a photograph and a schematic of the pressurized, fully-clamped plate with magnetization $\mathbf{M} = M\mathbf{e}_3$ under a magnetic field $\mathbf{B}^{\mathrm{a}} = B^{\mathrm{a}}\mathbf{e}_3$. Both $\mathbf{M}$ and $\mathbf{B}^{\mathrm{a}}$ are oriented perpendicularly to the plate mid-surface, differently from the configuration considered in Section 7.4.

Fig. 6(c) and (d) present the normalized deflection at the center of the plate, δ_z/h, versus the applied pressure, at three different fixed levels of magnetic flux density $B^{\mathrm{a}} = \{0, 80, 160\}\,\mathrm{mT}$. The experimental results are accurately reproduced by the **R**-based plate and 3D models (see Fig. 6c). The magnetic torques induced due to the deflection increase the resistance of the plate to the pressure loading. This effect becomes more prominent for stronger applied fields.

By contrast, in Fig. 6(d), we find that the **F**-based 3D model disagrees with experiments. In particular, the **F**-based 3D model predicts a significantly lower deflection than that obtained in the experiment, and that given by the **R**-based 3D and plate models. As reported by Zhao et al. (2019), according to the **F**-based theory, pre-stretches are induced in a free bulk MRE when the applied field is parallel to the magnetization. In our case, in-plane pre-stresses are induced in the mid-surface by the out-of-plane pre-stretch, since the plate is fully constrained. These magnetically-induced in-plane stresses, in addition to the magnetic torques due to the rotational deformation, further stiffen the plate, explaining the observation in Fig. 6(d) that the **F**-based 3D model underestimates the plate deflection. In contrast, the magnetically-induced pre-stretches and pre-stresses do not exist for the **R**-based models, since the magnetic potential is independent of stretching deformation. Based on this comparison against experiments, we conclude that the pre-stretches and pre-stresses predicted by the **F**-based theory are erroneous, and the source of the discrepancy with experiments.

In Fig. 6(d), we remark that the **F**-based plate model, which is identical to the **R**-based plate model in this specific configuration ($\mathbf{M} = M\mathbf{e}_3$, as mentioned in Section 4.5), agrees well with the experiments, even though it is reduced from a 3D model that

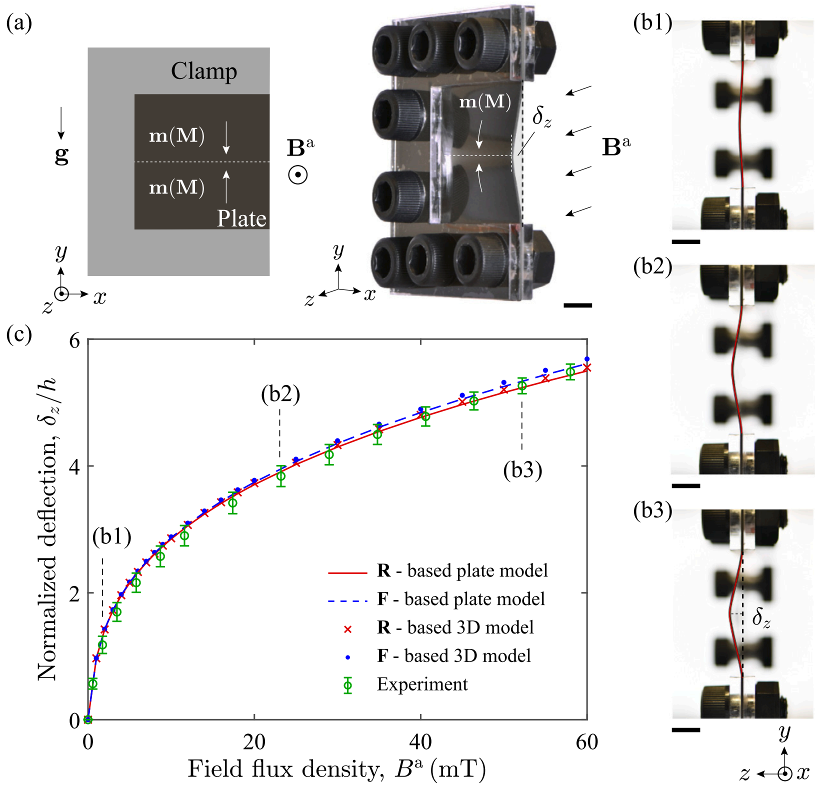

Fig. 4. Deformation of a plate clamped at three edges under a uniform magnetic field. (a) Left: Schematic diagram in the x–y plane. Right: Photograph of a plate specimen, with three edges clamped between rigid plates. The gravitational field **g** points in the $-y$ direction. (b) Experimental photographs (side view: $y-z$ plane) of the deformed plate at different levels of magnetic flux density: (b1) $B^a = 1.7\,\mathrm{mT}$, (b2) $B^a = 23\,\mathrm{mT}$, and (b3) $B^a = 52\,\mathrm{mT}$. The red lines in each photograph are the deformed configurations predicted by the **R**-based plate model. (c) Normalized deflection at the midpoint of the free edge, δ_z/h, versus magnetic flux density B^a. The error bars correspond to the standard deviations of the measurements on three identical specimens. The labeled points correspond to the photographs in (b1), (b2), and (b3) for the respective values of B^a. The dimensions of the specimen are provided in Table 1.

itself yields incorrect predictions. This contradiction can be attributed to the Kirchhoff–Love assumption applied when deriving the kinematics of thin plates through dimensional reduction. This assumption eliminates any out-of-plane deformation, thus removing the artificial pre-stretch in the out-of-plane direction. Hence, no in-plane pre-stresses are induced in the plate mid-surface.

8. Conclusion

We studied hard-MRE plates and developed models for their deformation under combined magnetic and mechanical loading. Our plate model was derived through the dimensional reduction of a 3D continuum, adapting the torque-based theory of hard-MREs (Zhao et al., 2019). Our modified 3D theory accounts for the composite nature of the MRE. In particular, we related the magnetizations in the initial and deformed configurations using only the rotation tensor **R**, decomposed from the deformation gradient **F**, yielding a **R**-based expression of the magnetic potential. Our reformulation was inspired by the recent work of Mukherjee et al. (2021), where the magnetization of saturated incompressible hard-MREs was shown to be independent of stretching.

We devised several test cases to assess the performance of the proposed 3D and 2D models through experiments involving large deflections and stretching. The predictions from the **R**-based models are in excellent agreement with experiments, for all the cases we considered. As opposed to the **R**-based models, the **F**-based 2D and 3D models sometimes failed to predict the deformation of hard-MRE plates. In particular, when non-negligible stretching deformation is present, errors are induced due to the incorrect description of the magnetization of the deformed plate. These disparities are most significant when the applied field is parallel to the initial magnetization of the plate. We explained the disagreement between the existing **F**-based theory and the experiments by the magnetically induced pre-stretches/stresses that can be mistakenly predicted in a free/constrained hard-MRE (Zhao et al., 2019). We also showed how the Kirchhoff–Love assumption can artificially correct this discrepancy in the **F**-based plate model. To the best of our knowledge, this is the first experimental validation of a rotation-based model for hard-MREs, here in a plate geometry.

The proposed plate model could enable the systematic exploration of the design space of more complex problems while providing physical insight through analysis of the reduced energy potential. Our geometrically nonlinear plate model can be used as a basis to develop simpler versions through additional assumptions on the extents of strains and rotations. When deriving the reduced magnetic potential in Eq. (18), for simplicity, only the zero-order term was retained. The appropriateness of this approximation is

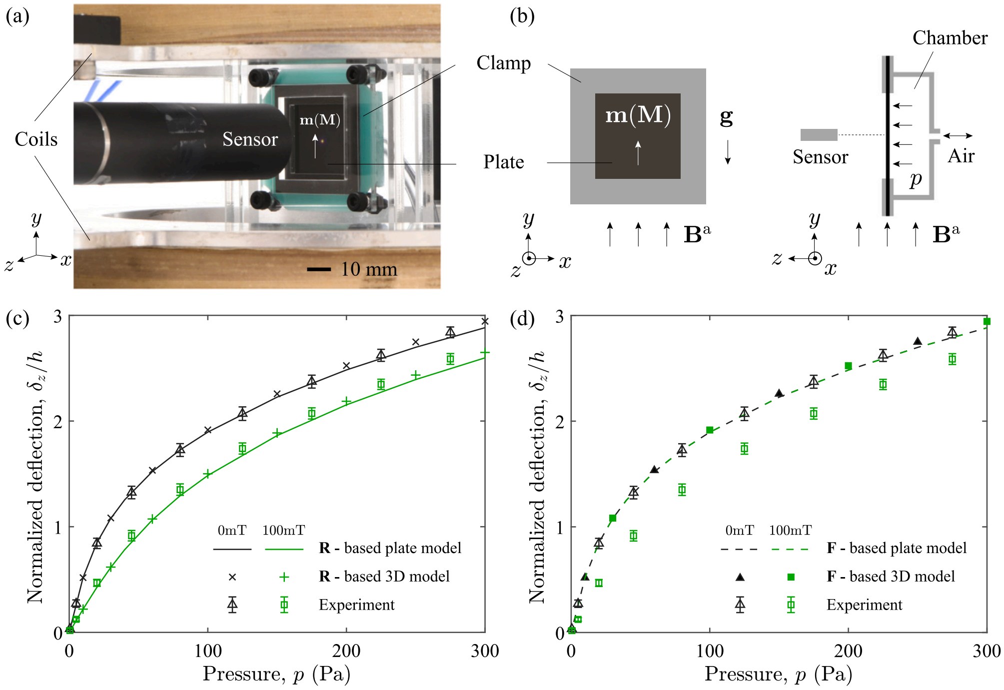

Fig. 5. Deformation of a fully-clamped plate with *in-plane* magnetization under combined pressure and magnetic loading. (a) Photograph of a plate specimen positioned in between the Helmholtz coils. The deflection at the plate center was measured by an optical position sensor. (b) Schematic of the configuration considered in the experiment. The pressure loading was imposed on the plate by changing the air pressure in the chamber. (c,d) Normalized deflection at the center of the plate, δ_z/h, versus imposed pressure, p, at magnetic flux density $B^a = \{0, 100\}$ mT. The error bars correspond to the standard deviations of the measurements on three identical specimens.

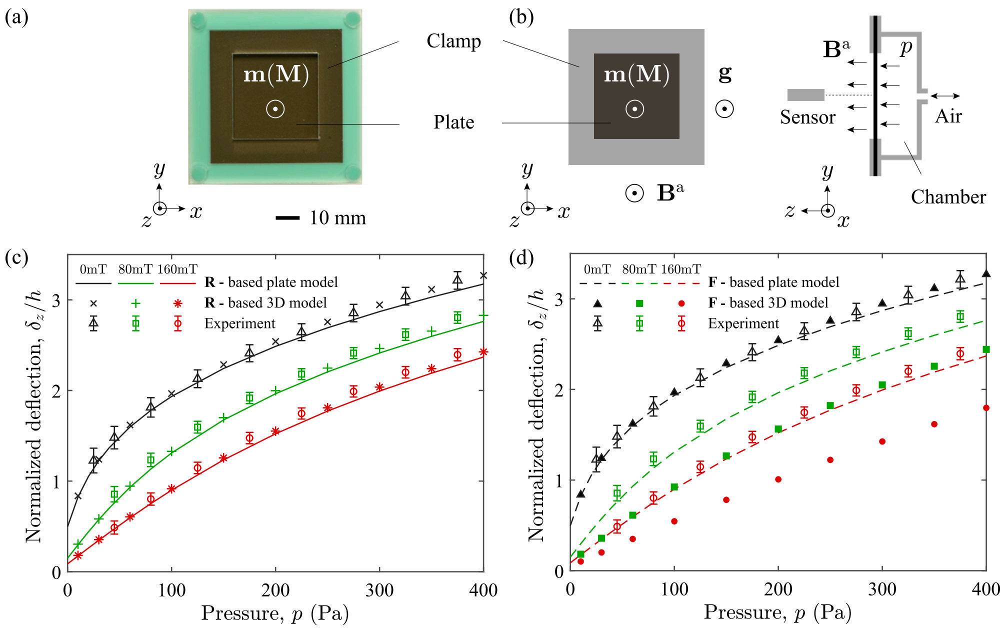

Fig. 6. Deformation of a fully-clamped plate with *out-of-plane* magnetization under combined pressure and magnetic loading. (a) Photograph of a plate specimen clamped at its four edges. (b) Schematic of the configuration considered in the experiment. The pressure loading was imposed on the plate by changing the air pressure in the chamber. (c,d) Normalized deflection δ_z/h at the center of the plate, versus imposed pressure, p, at different levels of applied magnetic flux density $B^a = \{0, 80, 160\}$ mT. The initial deflections in experiments at $p = 0$ due to gravity were characterized using an optical profilometer (VR-3200, Keyence). The error bars correspond to the standard deviations of the measurements on three identical specimens.

corroborated by the excellent agreement we found between the plate model and experiments on the test cases considered. However, retaining high-order terms may be needed in problems involving larger stains or non-uniform fields. We also note that in more complex scenarios, when self-interactions, magnetic hysteresis, or viscoelastic effects of the MRE are non-negligible, the 3D models developed by Mukherjee et al. (2021) and Rambausek et al. (2022) should be preferred over ours. Finally, when the MRE is not subjected to significant stretching, the **F**-based model of Zhao et al. (2019) remains appropriate, as verified by the results from our first three test cases.

Our work provides a theoretical framework for future studies on the mechanics of hard-magnetic plates. Potential new directions for research include magnetic plate buckling, and the rational design of reconfigurable plate-like structures through magneto-elastic effects. With recent research in MREs gearing towards biomedical applications (Wang et al., 2022; Kim and Zhao, 2022), where precise modeling and closed-loop control are often required, we also believe that our 3D, rotation-based model is timely, providing an accurate and efficient modeling framework for hard-MREs.

CRediT authorship contribution statement

Dong Yan: Conceptualization, Methodology, Validation, Investigation, Formal analysis, Software, Writing – original draft, Writing – review & editing. **Bastien F.G. Aymon:** Conceptualization, Methodology, Validation, Investigation, Formal analysis, Writing – review & editing. **Pedro M. Reis:** Conceptualization, Methodology, Supervision, Writing – review & editing.

Declaration of competing interest

The authors declare that they have no known competing financial interests or personal relationships that could have appeared to influence the work reported in this paper.

Data availability

Data will be made available on request.

Acknowledgment

The authors are grateful to Matteo Pezzulla for his help in setting up the 2D simulations in COMSOL, building up on his previous work from Pezzulla et al. (2022).

Appendix A. Inverse of stretch tensor $\mathbf{U}^{-1}$

The expression of the inverse of stretch tensor $\mathbf{U}^{-1}$ in terms of deformation gradient $\mathbf{F}$ of a continuum can be found in (Hoger and Carlson, 1984; Sawyers, 1986; Guan-Suo, 1998):

$$\begin{aligned}\mathbf{U}^{-1} = & \left(I_3^{\mathbf{U}}\Delta^{\mathbf{U}}\right)^{-1}\left\{\left[I_1^{\mathbf{U}}\left(I_2^{\mathbf{U}}\right)^2 - I_3^{\mathbf{U}}\left(I_1^{\mathbf{U}}\right)^2 - I_3^{\mathbf{U}}I_2^{\mathbf{U}}\right]\mathbf{I}\right.\\ & \left. - \left[I_3^{\mathbf{U}} + \left(I_1^{\mathbf{U}}\right)^3 - 2I_1^{\mathbf{U}}I_2^{\mathbf{U}}\right]\mathbf{C} + I_1^{\mathbf{U}}\mathbf{C}^2\right\},\end{aligned} \tag{A.1}$$

where $\Delta^{\mathbf{U}} = I_1^{\mathbf{U}}I_2^{\mathbf{U}} - I_3^{\mathbf{U}}$ and $\mathbf{C} = \mathbf{F}^{\mathrm{T}}\mathbf{F}$. The three principal invariants of $\mathbf{U}$, $I_1^{\mathbf{U}}$, $I_2^{\mathbf{U}}$, and $I_3^{\mathbf{U}}$, are also given in (Hoger and Carlson, 1984; Sawyers, 1986; Guan-Suo, 1998)

$$\begin{aligned}I_1^{\mathbf{U}} &= \sqrt{I_1^{\mathbf{C}} + 2I_2^{\mathbf{U}}},\\ I_2^{\mathbf{U}} &= \frac{\sqrt{2\sqrt{I_3^{\mathbf{C}}}\lambda^3 + I_2^{\mathbf{C}}\lambda^2 - I_3^{\mathbf{C}}} + \sqrt{I_3^{\mathbf{C}}}}{\lambda},\\ I_3^{\mathbf{U}} &= \sqrt{I_3^{\mathbf{C}}},\end{aligned} \tag{A.2}$$

where $I_1^{\mathbf{C}}$, $I_2^{\mathbf{C}}$, and $I_3^{\mathbf{C}}$ are the three principal invariants of $\mathbf{C}$, and

$$\lambda = \frac{1}{\sqrt{3}}\left\{I_1^{\mathbf{C}} + 2\left[\left(I_1^{\mathbf{C}}\right)^2 - 3I_2^{\mathbf{C}}\right]^{\frac{1}{2}}\cos\left[\frac{1}{3}\cos^{-1}\left(\frac{2\left(I_1^{\mathbf{C}}\right)^3 - 9I_1^{\mathbf{C}}I_2^{\mathbf{C}} + 27I_3^{\mathbf{C}}}{2\left(I_1^{\mathbf{C}}I_1^{\mathbf{C}} - 3I_2^{\mathbf{C}}\right)^{\frac{3}{2}}}\right)\right]\right\}^{\frac{1}{2}}. \tag{A.3}$$

Appendix B. Magnetic potential reduced from the F-based 3D theory

To specialize the 3D magnetic potential in Eq. (5) of the **F**-based 3D theory for thin plates, we plug the deformation gradient **F** from Eq. (11) into Eq. (5):

$$U_{\mathbf{F}}^{\mathrm{m}} = -J^{-1}(\hat{\mathbf{F}}\mathbf{M}) \cdot \mathbf{B}^{\mathrm{a}} - \eta_3 J^{-1}[(\mathbf{n}_{,\alpha} \otimes \mathbf{e}_\alpha)\mathbf{M}] \cdot \mathbf{B}^{\mathrm{a}} . \tag{B.1}$$

Eq. (B.1) is then integrated over the thickness ($\eta_3 \in [-h/2,\, h/2]$) to yield the reduced 2D magnetic potential of a thin plate defined with respect to its mid-surface

$$\hat{U}_{\mathbf{F}}^{\mathrm{m}} = -h(\hat{\mathbf{F}}\mathbf{M}) \cdot \mathbf{B}^{\mathrm{a}} . \tag{B.2}$$

To obtain this result, we have assumed that **M** and $\mathbf{B}^{\mathrm{a}}$ are constant along the thickness, and we note that the first-order term vanishes after the integration over η_3. The 2D formulation in Eq. (B.2) is the reduced magnetic potential for the **F**-based plate model.

References

Alapan, Y., Karacakol, A.C., Guzelhan, S.N., Isik, I., Sitti, M., 2020. Reprogrammable shape morphing of magnetic soft machines. Sci. Adv. 6, eabc6414.
Argyris, J.H., Fried, I., Scharpf, D.W., 1968. The TUBA family of plate elements for the matrix displacement method. Aeronaut. J. 72 (692), 701–709.
Audoly, B., Pomeau, Y., 2010. Elasticity and Geometry: from Hair Curls to the Non-Linear Response of Shells. Oxford University Press.
Brown, W.F., 1966. Magnetoelastic Interactions. In: Springer Tracts in Natural Philosophy, vol. 9, Springer, Berlin, Heidelberg.
Chen, T., Pauly, M., Reis, P.M., 2021. A reprogrammable mechanical metamaterial with stable memory. Nature 589, 386–390.
Danas, K., Kankanala, S.V., Triantafyllidis, N., 2012. Experiments and modeling of iron-particle-filled magnetorheological elastomers. J. Mech. Phys. Solids 60, 120–138.
Dorfmann, A., Ogden, R.W., 2003. Magnetoelastic modelling of elastomers. Eur. J. Mech. A 22, 497–507.
Dorfmann, A., Ogden, R., 2004. Nonlinear magnetoelastic deformations of elastomers. Acta Mech. 167, 13–28.
Dorfmann, A., Ogden, R.W., 2005. Some problems in nonlinear magnetoelasticity. Z. Angew. Math. Phys. 56, 718–745.
Garcia-Gonzalez, D., 2019. Magneto-visco-hyperelasticity for hard-magnetic soft materials: theory and numerical applications. Smart Mater. Struct. 28, 085020.
Garcia-Gonzalez, D., Hossain, M., 2021. Microstructural modelling of hard-magnetic soft materials: Dipole–dipole interactions versus Zeeman effect. Extreme Mech. Lett. 48, 101382.
Ginder, J.M., Nichols, M.E., Elie, L.D., Clark, S.M., 2000. Controllable-stiffness components based on magnetorheological elastomers. In: Smart Structures and Materials 2000: Smart Structures and Integrated Systems, Vol. 3985. SPIE, pp. 418–425.
Ginder, J.M., Schlotter, W.F., Nichols, M.E., 2001. Magnetorheological elastomers in tunable vibration absorbers. In: Smart Structures and Materials 2001: Damping and Isolation, Vol. 4331. SPIE, pp. 103–110.
Gray, B.L., 2014. A review of magnetic composite polymers applied to microfluidic devices. J. Electrochem. Soc. 161, B3173.
Gu, H., Boehler, Q., Cui, H., Secchi, E., Savorana, G., De Marco, C., Gervasoni, S., Peyron, Q., Huang, T.-Y., Pane, S., Hirt, A.M., Ahmed, D., Nelson, B.J., 2020. Magnetic cilia carpets with programmable metachronal waves. Nature Commun. 11, 2637.
Guan-Suo, D., 1998. Determination of the rotation tensor in the polar decomposition. J. Elasticity 50 (3), 197–207.
Hoger, A., Carlson, D.E., 1984. Determination of the stretch and rotation in the polar decomposition of the deformation gradient. Q. Appl. Math. 42 (1), 113–117.
Hu, W., Lum, G.Z., Mastrangeli, M., Sitti, M., 2018. Small-scale soft-bodied robot with multimodal locomotion. Nature 554, 81–85.
Kankanala, S.V., Triantafyllidis, N., 2004. On finitely strained magnetorheological elastomers. J. Mech. Phys. Solids 52, 2869–2908.
Kim, Y., Parada, G.A., Liu, S., Zhao, X., 2019. Ferromagnetic soft continuum robots. Sci. Robot. 4, eaax7329.
Kim, Y., Yuk, H., Zhao, R., Chester, S.A., Zhao, X., 2018. Printing ferromagnetic domains for untethered fast-transforming soft materials. Nature 558, 274.
Kim, Y., Zhao, X., 2022. Magnetic soft materials and robots. Chem. Rev. 122, 5317–5364.
Kordonsky, W.I., 1993. Magnetorheological effect as a base of new devices and technologies. J. Magn. Magn. Mater. 122, 395–398.
Kuang, X., Wu, S., Ze, Q., Yue, L., Jin, Y., Montgomery, S.M., Yang, F., Qi, H.J., Zhao, R., 2021. Magnetic dynamic polymers for modular assembling and reconfigurable morphing architectures. Adv. Mater. 33, 2102113.
Lum, G.Z., Ye, Z., Dong, X., Marvi, H., Erin, O., Hu, W., Sitti, M., 2016. Shape-programmable magnetic soft matter. Proc. Natl. Acad. Sci. USA 113, E6007–E6015.
Mukherjee, D., Bodelot, L., Danas, K., 2020. Microstructurally-guided explicit continuum models for isotropic magnetorheological elastomers with iron particles. Int. J. NonLinear Mech. 120, 103380.
Mukherjee, D., Rambausek, M., Danas, K., 2021. An explicit dissipative model for isotropic hard magnetorheological elastomers. J. Mech. Phys. Solids 151, 104361.
Pao, Y.-H., 1978. IV - electromagnetic forces in deformable continua. In: Nemat-Nasser, S. (Ed.), Mechanics Today. Pergamon, pp. 209–305.
Pezzulla, M., Yan, D., Reis, P.M., 2022. A geometrically exact model for thin magneto-elastic shells. J. Mech. Phys. Solids 166, 104916.
Rambausek, M., Mukherjee, D., Danas, K., 2022. A computational framework for magnetically hard and soft viscoelastic magnetorheological elastomers. Comput. Methods Appl. Mech. Engrg. 391, 114500.
Sano, T.G., Pezzulla, M., Reis, P.M., 2022. A Kirchhoff-like theory for hard magnetic rods under geometrically nonlinear deformation in three dimensions. J. Mech. Phys. Solids 160, 104739.
Sawyers, K., 1986. Comments on the paper determination of the stretch and rotation in the polar decomposition of the deformation gradient by A. Hoger and D. E. Carlson. Q. Appl. Math. 44 (2), 309–311.
Schümann, M., Borin, D.Y., Morich, J., Odenbach, S., 2021. Reversible and non-reversible motion of NdFeB-particles in magnetorheological elastomers. J. Intell. Mater. Syst. Struct. 32, 3–15.
Tang, S.-Y., Zhang, X., Sun, S., Yuan, D., Zhao, Q., Yan, S., Deng, L., Yun, G., Zhang, J., Zhang, S., Li, W., 2018. Versatile microfluidic platforms enabled by novel magnetorheological elastomer microactuators. Adv. Funct. Mater. 28, 1705484.
Truesdell, C., Toupin, R., 1960. The classical field theories. In: Principles of Classical Mechanics and Field Theory / Prinzipien Der Klassischen Mechanik Und Feldtheorie. In: Encyclopedia of Physics / Handbuch der Physik, Springer, Berlin, Heidelberg, pp. 226–858.
Vaganov, M.V., Borin, D.Y., Odenbach, S., Raikher, Y.L., 2018. Effect of local elasticity of the matrix on magnetization loops of hybrid magnetic elastomers. J. Magn. Magn. Mater. 459, 92–97.
Vaganov, M.V., Borin, D.Y., Odenbach, S., Raikher, Y.L., 2020. Training effect in magnetoactive elastomers due to undermagnetization of magnetically hard filler. Physica B 578, 411866.
Wang, L., Kim, Y., Guo, C.F., Zhao, X., 2020. Hard-magnetic elastica. J. Mech. Phys. Solids 142, 104045.
Wang, Y., Liu, J., Yang, S., 2022. Multi-functional liquid crystal elastomer composites. Appl. Phys. Rev. 9, 011301.

Wang, L., Zheng, D., Harker, P., Patel, A.B., Guo, C.F., Zhao, X., 2021. Evolutionary design of magnetic soft continuum robots. Proc. Natl. Acad. Sci. USA 118, e2021922118.

Wu, S., Hu, W., Ze, Q., Sitti, M., Zhao, R., 2020. Multifunctional magnetic soft composites: a review. Multifunct. Mater. 3, 042003.

Yan, D., Abbasi, A., Reis, P.M., 2021a. A comprehensive framework for hard-magnetic beams: Reduced-order theory, 3D simulations, and experiments. Int. J. Solids Struct. http://dx.doi.org/10.1016/j.ijsolstr.2021.111319.

Yan, Y., Hu, Z., Yang, Z., Yuan, W., Song, C., Pan, J., Shen, Y., 2021c. Soft magnetic skin for super-resolution tactile sensing with force self-decoupling. Science Robotics 6, eabc8801.

Yan, D., Pezzulla, M., Cruveiller, L., Abbasi, A., Reis, P.M., 2021b. Magneto-active elastic shells with tunable buckling strength. Nature Commun. 12, 2831.

Yih-Hsing, P., Chau-Shioung, Y., 1973. A linear theory for soft ferromagnetic elastic solids. Internat. J. Engrg. Sci. 11, 415–436.

Ze, Q., Kuang, X., Wu, S., Wong, J., Montgomery, S.M., Zhang, R., Kovitz, J.M., Yang, F., Qi, H.J., Zhao, R., 2020. Magnetic shape memory polymers with integrated multifunctional shape manipulation. Adv. Mater. 32, 1906657.

Zhang, J., Ren, Z., Hu, W., Soon, R.H., Yasa, I.C., Liu, Z., Sitti, M., 2021. Voxelated three-dimensional miniature magnetic soft machines via multimaterial heterogeneous assembly. Sci. Robot. 6, eabf0112.

Zhang, R., Wu, S., Ze, Q., Zhao, R., 2020. Micromechanics study on actuation efficiency of hard-magnetic soft active materials. J. Appl. Mech. 87, 091008.

Zhao, R., Kim, Y., Chester, S.A., Sharma, P., Zhao, X., 2019. Mechanics of hard-magnetic soft materials. J. Mech. Phys. Solids 124, 244–263.